2016

Multicharged Carbon Ion Generation from Laser Plasma

Oguzhan Balki
Old Dominion University

Hani E. Elsayed-Ali
Old Dominion University, helsayed@odu.edu

Multicharged carbon ion generation from laser plasma

Oguzhan Balki and Hani E. Elsayed-Ali[a)]
Department of Electrical and Computer Engineering and the Applied Research Center, Old Dominion University, Norfolk, Virginia 23529, USA

Carbon ions generated by ablation of a carbon target using an Nd:YAG laser pulse (wavelength $\lambda = 1064$ nm, pulse width $\tau = 7$ ns, and laser fluence of 10-110 J cm^{-2}) are characterized. Time-of-flight analyzer, a three-mesh retarding field analyzer, and an electrostatic ion energy analyzer are used to study the charge and energy of carbon ions generated by laser ablation. The dependencies of the ion signal on the laser fluence, laser focal point position relative to target surface, and the acceleration voltage are described. Up to C^{4+} ions are observed. When no acceleration voltage is applied between the carbon target and a grounded mesh in front of the target, ion energies up to ~400 eV/charge are observed. The time-of-flight signal is analyzed for different retarding field voltages in order to obtain the ion kinetic energy distribution. The ablation and Coulomb energies developed in the laser plasma are obtained from deconvolution of the ion time-of-flight signal. Deconvolution of the time-of-flight ion signal to resolve the contribution of each ion charge is accomplished using data from a retarding field analysis combined with the time-of-flight signal. The ion energy and charge state increase with the laser fluence. The position of the laser focal spot affects the ion generation, with focusing ~1.9 mm in front of the target surface yielding maximum ions. When an external electric field is applied in an ion drift region between the target and a grounded mesh parallel to the target, fast ions are extracted and separated, in time, due to increased acceleration with charge state. *Published by AIP Publishing.* [http://dx.doi.org/10.1063/1.4966987]

I. INTRODUCTION

Multicharged ion (MCI) sources have uses in nanoprocessing, ion implantation, ion lithography, biomedicine, cancer therapy, and secondary ion mass-spectrometry.[1–3] In an MCI interaction, both its potential and kinetic energies are involved. The potential energy of highly charged ions can exceed their kinetic energy, particularly for ultraslow ions. When used for surface modification, MCIs with low kinetic energies have high surface selectivity causing strong local excitation not accessible with singly charged ions. An MCI interaction with a surface can trigger local surface modification by potential sputtering resulting in the formation of a nano-scale crater, a feature that may be useful for nanopatterning and nanoidentification.[4] The ability to independently control MCI potential and kinetic energies is useful for surface analysis and surface modification. MCI implantation in metals can modify the surface tension, hardness, and corrosion resistance.[2,5,6] Slow highly charged ions can be used in semiconductor surface processing due to their high potential energy combined with low kinetic energy which allows for localizing the ion potential energy at the surface. Using ultraslow Ar^{q+}, ($q > 1$) MCIs with high potential energy, native silicon oxide was removed from the Si surface with less surface damage than possible when singly charged Ar^{1+} ion is used.[7] After slow Ar MCI etching, the surface roughness was increased by only 0.05 nm root-mean-square (rms).[7]

The most developed sources of MCIs are electron beam ion sources (EBISs) and the electron cyclotron resonance ion sources (ECRISs).[8] Both EBIS and ECRIS generate MCIs from gases. Generating MCI from a solid target involves its vaporization and introduction of the vapor in the EBIS or ECRIS. Laser multicharged ion sources (LMCI) use laser ablation of a solid target to generate dense plasma containing MCIs. Thus, LMCI can operate in ultrahigh vacuum requiring only small pumping capacity. MCIs produced from laser plasma can provide a cost-effective add-on to existing pulsed laser deposition systems, generate MCI pulses, and reduce MCI equipment size and cost.[9] Several groups have studied laser generated MCIs. Mróz *et al.* reported on the generation of Ta, Al, and Cu MCIs with iodine laser ($\lambda = 1315$ nm and $\tau = 350$ ps) with an intensity up to 10^{15} W cm^{-2}. The maximum charge states they obtained were Cu^{22+}, Ta^{9+}, and Al^{13+}.[10] Al MCIs up to Al^{4+} were obtained at maximum laser intensity of 8.7×10^{10} W cm^{-2} with Nd:YAG laser ($\lambda = 1064$ nm).[11] Henkelmann *et al.* used CO$_2$ and Nd:YAG lasers ($\lambda = 10.6$ μm and 1064 nm, respectively) together to show the influence of the combined laser interaction with a solid Ta target.[12] The charge state generation increased from Ta^{11+} to Ta^{13+} depending on the delay between the laser pulses. The CO$_2$ laser increased the electron temperature in the expanding plasma reducing the recombination rate resulting in increased extraction of higher charge states. Nassisi *et al.* reported using low energy XeCl excimer laser ($\lambda = 308$ nm) pulses to produce MCIs from a Cu solid target.[13] The MCI generation was strongly dependent on the focal lens used for the same laser fluence on target. Using a lens with 15 cm focal length, the maximum total charge observed was ~0.035 μC for a laser fluence of 17 J cm^{-2}.

a)Author to whom correspondence should be addressed. Electronic mail: helsayed@odu.edu. Tel.: (757)269-5645.

Up to Cu^{5+} was observed when the different charges were separated by a 30 kV acceleration voltage. Lorusso et al. used a XeCl excimer laser ($\lambda = 308$ nm, $\tau = 20$ ns, pulse energy $= 70$ mJ, and intensity $= 3.5 \times 10^8$ W cm^{-2}) to study the charge extraction characteristics of the generated Cu^{q+} ion pulses.[14]

Laser ablation was previously used to generate carbon MCIs.[15–20] Kashiwagi et al. reported the observation of fully stripped C^{6+} ions using Nd:YAG ($\lambda = 1064$ nm, $\tau = 15$ ns, pulse energy $= 400$ mJ, and intensity $= 1.6 \times 10^{11}$ W cm^{-2}). The ions were injected into a radio frequency quadruple linac. The total number of C^{6+} ions injected into the linac was 6.0 $\times 10^9$ with a current of 17 mA.[15] Emission of C MCIs was reported for CO_2 laser ($\lambda = 10.6$ μm, $\tau = 85$ ns, and fluence of 1.2 J cm^{-2}).[16] An electrostatic deflector ion filter was used to analyze the carbon ions with ion charge up to C^{5+} reported. Constantinescu et al. reported on the interaction of C_{60} molecules with ultrashort high-intensity femtosecond laser pulses ($\lambda = 790$ nm) with an intensity of 10–1000 TW cm^{-2}. Carbon ions up to C^{4+} were produced.[17] Witanachchi et al. produced carbon plasma with C^{1+} and C^{2+} using a combination of an excimer KrF laser ($\lambda = 248$ nm) and a CO_2 laser ($\lambda = 10.6$ μm) suggesting the ionization, kinetic energy of ions, and the plasma temperature increase when two lasers are used.[18] Torrisi et al. studied MCI generation from ablation of graphite by frequency-doubled Nd:YAG laser ($\lambda = 532$ nm and $\tau = 3$ ns). At a fluence of 5.7 J cm^{-2}, up to C^{4+} ions were detected. Ion acceleration by ~85 eV/charge state was measured.[19] Okihara et al. reported C^{4+} ions above 5 MeV/charge state using Ti:sapphire laser system ($\lambda = 815$ nm, 2.4×10^{12} W, maximum intensity $= 3 \times 10^{18}$ W cm^{-2}, and $\tau = 50$ fs).[20]

Carbon ions have applications in thin film deposition, semiconductor processing, ion implantation, and radiotherapy. Carbon ions implantation into the floating gate surface is used in flash memory devices that minimizes the polysilicon grain growth and smooths the surface.[21] This helps to reduce the interfacial trap density and improves the integrity and uniformity of the thin dielectrics deposited between the floating and polysilicon gates of nonvolatile memory devices. Carbon implantation into Ti–6Al–4V alloy enhances surface wear resistance, increases hardness due to TiC formation, and reduces the surface friction coefficient.[22] Simultaneous implantation with different charge carbon ions results in a plateau like depth profile that is dependent on the ion energy distribution.[22] Graphite-like carbon (GLC) has uses as a coating material, offering high hardness and high flexibility required in implants such as in artificial joints.[23] Carbon ions have more favorable dose-depth distribution than photons and are the new frontiers of cancer therapy.[24,25] The use of carbon ions in radiotherapy results in localized energy targeting hard-to-reach tumors with minimum effects to other tissues. Fully stripped C^{6+} ions are used in radiotherapy because of the relative ease in their acceleration, bending, and focusing and their high potential energy which can be deposited in a localized volume.[25]

We report on carbon LMCI source using a Nd:YAG laser ($\lambda = 1064$ nm and $\tau = 7$ ns). The charge state and energy of carbon MCIs are studied by a time-of-flight (TOF) analyzer, a three-mesh retarding field analyzer (RFA), and an electrostatic ion energy analyzer (EIA). Charge states up to C^{4+} were observed with laser pulse energy of 34 mJ. Ion energy distributions are measured using an EIA that selects ions with different energy-to-charge. The dependencies of the carbon ions extracted from the laser plasma on the laser pulse energy, laser focal spot position, and external accelerating electric field are studied. Carbon MCI generation was previously reported.[15,17,19,20] The present work extends previous studies by measuring the energy distribution of each carbon ion charge using an energy-to-charge (E/z) electrostatic ion energy analyzer (EIA). The ion energy follows a shifted Maxwell–Boltzmann distribution that is dependent on the ablation velocity and Coulomb potential developed in the double layer (DL) of the expanding laser plasma.[26] Calculations of carbon ions energy distribution are critical for the carbon ion implantation of materials aiming to change surface properties. The deconvolution of time-of-flight (TOF) ion signal using data obtained from the retarding field analysis allows us to resolve the ion signal from each charge more accurately than solely from the TOF signal. Also, we show that the position of the lens focusing the laser on target affects carbon ion yield and ion energy distribution.

II. EXPERIMENTAL SETUP

The carbon MCIs are generated in a vacuum chamber schematically shown in Fig. 1. A Q-switched Nd:YAG laser (Continuum Surelite SL I-10, $\lambda = 1064$ nm, $\tau = 7$ ns) was used to ablate a glassy carbon disc target of 99.99% purity, 0.58 mm thickness, <50 nm surface roughness, as characterized by the manufacturer (HTW, Germany). The laser is focused inside the chamber using a plano-convex lens to a diameter of ~200 μm at focus, as measured by the knife edge method at the target equivalent plane. The lens was mounted on a translational stage to allow for changing the position of focus relative to target surface. The laser pulse enters the chamber through a BK7 viewport and is incident on the target at an angle of 60° from the target normal. The laser pulse energy was varied by a combination of a half-waveplate and a thin film polarizer. The laser pulse energy was 4-38 mJ measured before the chamber window and the reported values were adjusted for the 8% loss in the glass window. The target was mounted on insulated
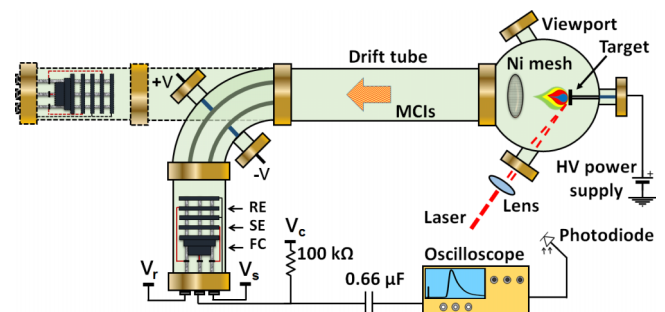
FIG. 1. A schematic diagram of the laser multicharged ion (LMCI) chamber equipped with drift tube, electrostatic ion energy analyzer (EIA), three-mesh retarding field analyzer (RFA), and time-of-flight (TOF) analyzer. V_r, V_s, V_c: Biasing for retarder electrode (RE), suppressor electrode (SE), and Faraday cup (FC). The system can be configured with and without the electrostatic ion energy analyzer (EIA) while maintaining the same distance between the target and the Faraday cup.

support to allow for applying an acceleration voltage while maintaining the chamber grounded. The chamber pressure was about 6×10^{-8} mbar; therefore, the loss of MCIs by charge transfer with the background gas is negligible.[27] The Faraday cup is placed 1.54 m away from the carbon target. The ion drift tube had a 10-cm inner diameter. Grounded nickel mesh 8 cm in diameter with an open area of 70% is placed 10 cm in front of the surface of the carbon disk.

The TOF detection consists of a 5-cm diameter Al Faraday cup with a suppressor ring electrode placed 1 cm away from the Faraday cup entrance. The MCI signal is detected with the Faraday cup biased at -80 V. We observed the shape of the MCI signal as we changed the suppressor voltage from -80 V to more negative values. Applying -120 V resulted in an all positive single-peaked pulse. Applying more negative voltage did not change the shape of the pulse. Therefore, applying -120 V to the suppressor ring was adequate to suppress the secondary electron emission from the Faraday cup due to positive ion collisions. This suppressor voltage was maintained throughout the experiment. The retarding field ion energy analyzer (RFA) consists of three 5-cm in diameter nickel grids with 70% open area separated by 1 cm. The two outer grids were grounded while the central grid was held at a variable voltage, V_r. The central retarding electrode was positively biased to analyze the extracted ion energy distribution. An oscilloscope (Tektronix DPO 3034, 50 Ω termination) was used to record ion signals through a 0.66 μF coupling capacitor. In order to compensate for pulse-to-pulse fluctuations, 20 consecutive laser pulses hitting the same target spot were averaged. For our experimental conditions, the shot-to-shot fluctuations of total ion yield were up to ~20%. However, no noticeable decline in the averaged ion signal was observed when hitting the same spot with up to 60 shots.

In experiments observing the MCIs with selected energy-to-charge ratio, E/z, part of the straight connection was replaced with the EIA maintaining the ion drift length the same as without the EIA. The EIA has a radial cylindrical design with a deflection angle of 90°. EIA analyzer has a range of E/z obtained by the relation $E/z = eR_0 E_r(R_0) = eU/(2 \ln(R_2/R_1)) \approx keU$,[28] where E is the kinetic energy of the ion, e is the unit charge E_r is the radial electric field inside the deflection plates, R_0 is the mean radius, U is the potential across the deflection plates, and $\kappa = R_0/2\Delta R$ is the geometric factor. EIA has an inner radius, R_1 of 5.69 in. and outer radius, R_2 of 7.19 in. The energy resolution $\Delta E/E$ was determined to be 7%–10% because no slit was used on both ends of the EIA.

III. RESULTS AND DISCUSSION

The laser-generated carbon ions are detected by the Faraday cup. The experimental results are divided into two sections. In Section III A, the carbon ions are generated without any acceleration voltage applied to the target; while in Section III B, the target is positively biased, which introduces an external electric field between the target and the grounded mesh that is located parallel to the target. The effects of laser pulse energy, laser focal point location relative to target surface, and the applied voltage on target are studied.

A. Plasma ions emitted without external acceleration

1. Analysis of multicharged ions with retarding field analyzer

When no voltage is applied to the target, the ions generated in the laser plasma are accelerated only by the plasma expansion and the internal electric field developed in the expanding plasma. A retarding field energy analyzer combined with time-of-flight ion spectra is used to probe the energy-to-charge E/z of the carbon ions and resolve the ion charge state z. The retarding potential modifies the ion signal displaying cut-offs in the signal that are dependent on z. With the increase in the retarding potential, different ions are stopped at a threshold value of v_{th}^2 described as $v_{th}^2 = 2zeV_r/m$.[13] V_r is defined as the retarding potential, m is the mass of carbon in kg, and e is the unit charge in Coulomb. The retarder potential stops all ions having kinetic energy below zeV_r. Higher charge state ions gain more kinetic energy when they are accelerated in the internal electric field of the expanding plume, thus are detected earlier by the Faraday cup. Regardless of the target material, a temporal distribution of charge states is observed in the extracted ions.

The TOF carbon ion signal observed for different retarding potentials is shown in Fig. 2. Similar analysis using a 3-grid retarding field analyzer was previously reported for Cu MCIs generated using excimer laser ablation.[13] The positive fast signal observed near time zero is due to the photoelectric effect where photons generated from the laser plasma with energy above the work function of the Faraday cup material cause electron emission. The inset in Fig. 2(a) is a closer look at the effect of retarder potential on carbon ion signal for the range of 180-300 V. Ions with lower kinetic energy than the applied retarding potential are blocked, whereas ions with higher kinetic energy lose some of their energy then, between the central and final grid, are accelerated back to their energy before entering the RFA. For instance, the cut-off at ~20 μs corresponds to C^{2+} ions with lower energy than $2eV_r$ (150 V retarding potential), whereas the cut-off at ~17 μs corresponds to C^{3+} ions with energy lower than $3eV_r$ (180 V retarding potential). The cut-off at ~11 μs corresponds to the C^{4+} ions with lower energy than $4eV_r$ (210 V retarding potential). The time at which the cut-offs are observed gets shorter with increasing the retarding potential. The knee in the ion signal at ~18 μs or more for various retarding potentials is ascribed to C^{1+} ions with energies lower than eV_r. Fig. 2(b) shows the square threshold velocity v_{th}^2 as a function of the retarding voltage. The corresponding threshold velocity for each cut-off in the plasma signal is calculated by dividing the ion propagation length by the cut-off time. Depending on the z, modified ion signals display cut-offs, which are used to calculate v_{th}^2 for each data point in Fig. 2(b). Using a linear fit to the experimental data, the values for each slope were calculated giving charge state information. This analysis revealed that carbon ions up to C^{4+} were detected by the Faraday cup. The total ion charge reaching the Faraday cup is obtained from $Q_i = (\int V_F(t)dt)/R$, where $V_F(t)$ is the voltage signal in the Faraday cup, and R is the 50 Ω oscilloscope internal resistance. The inset in Fig. 2(b) shows the total charge reduction with the increase of retarding potential. Total charge decreases from
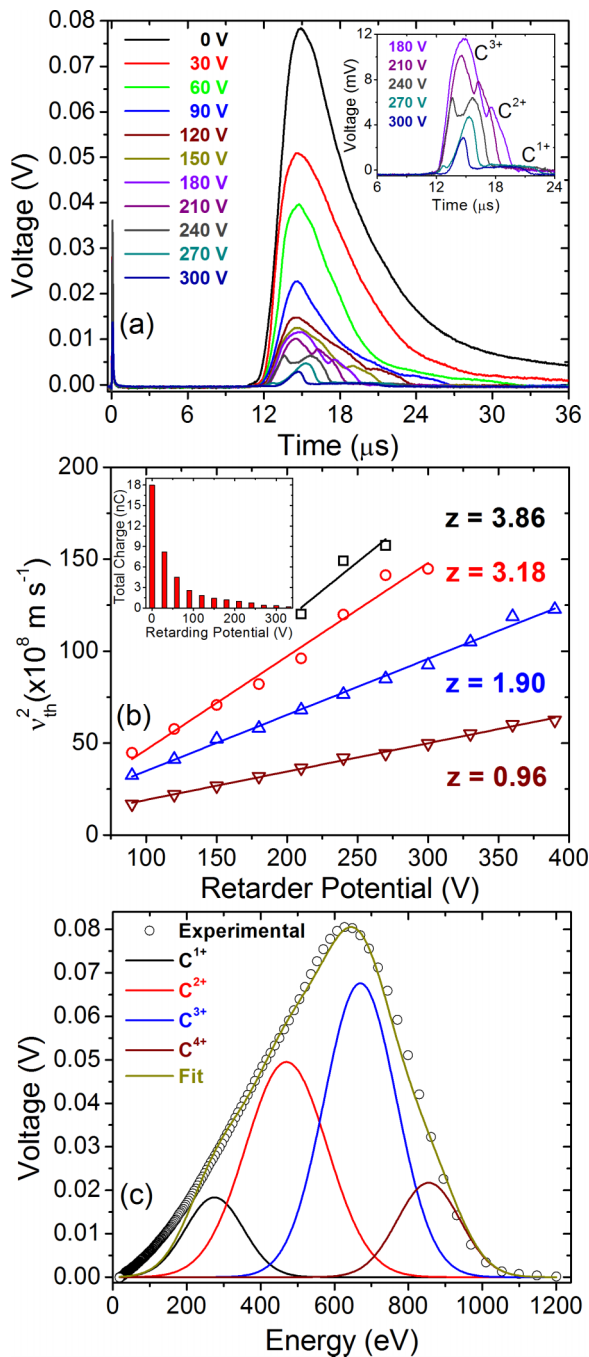
FIG. 2. (a) Carbon ion signal for various retarding voltages. *Inset*: the effect of the retarder potential on the stopping of different charges. (b) Charge state z is determined from the slope of v_{th}^2 versus retarding potential. *Inset*: total ion charge with the increase of retarding potential. (c) Deconvolution of energy spectrum for carbon ion species showing energy distributions up to C^{4+}.

~18 nC to ~0 nC when the retarding potential is set to ~460 V. The value of Q_i does not account for the ion loss in the extraction grid and the three grids of the RFA. Fig. 2(c) shows the energy spectrum of the carbon ions when no retarding field is applied. In order to determine the best fitting parameters to the ion signal, we used the information obtained from retarding field analysis in selecting the parameters used in the fit. The deconvolution was obtained for charge states up to C^{4+} since this was the highest charge state observed at this laser energy.

Knowing the retardation potential which retards a subgroup of ions, we can construct the ion energy distribution width and introduce this into the fitting parameters. This information was used for all charges when fitting parameters in Fig. 2(c) are defined. In the plasma core, fast electrons develop a double layer (DL) that splits different charge states, generating a self-consistent ambipolar electric field (double layer), which is primarily responsible for ions acceleration. The role played by prompt electrons in ion acceleration was previously studied.[29] Prompt electron emission from the plasma leaves a positive ion layer in the plasma-vacuum interface and during their escape repels some of the electrons in the plasma. With the increase in the initial electron density at the front of the expanding plasma, a condition can be reached where the ion oscillation frequency is not sufficient to compensate for electron compression in the plasma by the forces of the prompt electrons. This effect was concluded to lead to ion cloud fragmentation and a complex ion acceleration mechanism.[29] Thermal interactions, coulomb interactions, isothermal, and adiabatic expansion in vacuum are also responsible for accelerating the ions in plasma.[30] The drift and expansion of carbon plasma in our experiment can be attributed to the adiabatic expansion due to the Knudsen layer.

In a laser produced plasma, the Knudsen layer is formed within a few particle free paths near the target surface in which as few as 3 collisions per particle occurs.[31] Particles vaporized, sputtered, or desorbed reach equilibrium with each other within the Knudsen layer formed in a near-surface region during the laser ablation due to strong gas-phase interactions. This leads to a directional expansion perpendicular to the target surface. The ions are freely drifting into the vacuum, and ion charge-states are frozen at large distances. A shifted Maxwell–Boltzmann distribution due the collisions between ions during the initial phase of the plasma expansion can characterize the motion of ions far from the target. The ion current can be expressed with shifted Maxwell–Boltzmann distribution for the ion current analysis.[31,32] For laser plasma, the adiabatic expansion velocity (ablation) can be defined as $u_f = 2C_0/\gamma - 1$, where $C_0 = (\gamma kT/m)^{1/2}$ is the sound speed at the surface, where T refers to the Knudsen layer temperature, and γ is given as 1.3 for monoatomic species.[26] Using this equation, and taking $T = 20\,000$ K, ablation velocity is found to be $u_f = 4 \times 10^4$ m/s, or 99 eV as ablation energy. If we consider that the ions with different charges have energies corresponding to the sum of that due to the adiabatic expansion $E_{ablation}$ plus energy gain due to acceleration in the double layer by the Coulomb potential $E_{Coulomb}$, then the ion energy E is $E = E_{ablation} + zE_{Coulomb}$, where z is the ion charge. By fitting this equation to the experimental results, we calculate the ablation and coulomb energies as 80 and 195 eV, respectively. Bulgakova *et al.* reported similar calculations using a graphite target ablated with Nd:YAG laser operating at 1064 nm wavelength with 13 ns pulse width and laser fluence below 25 J cm^{-2} using T up to 4 eV. In their study, T was found to vary in the range ~2 to 8 eV for laser-generated carbon plasmas with laser intensities of 10^9–10^{10} W cm^{-2} for 70 ns pulses.[26] Harilal *et al.* reported an electron temperature of 1.45 eV at a distance of 3 mm from the target for carbon plasma with a laser intensity of 2.8×10^{10} W cm^{-2}.[33]

2. Laser energy dependence

The carbon ions were detected by their time-of-flight signal for different laser pulse energies applied to the target. All measurements were conducted with all other conditions kept constant. Results are shown in Fig. 3(a). The ion signal has a well-defined single peak at the high laser energies used. There is an apparent reduction of the arrival time of the fast ion peak with the increase in the laser pulse energy. The
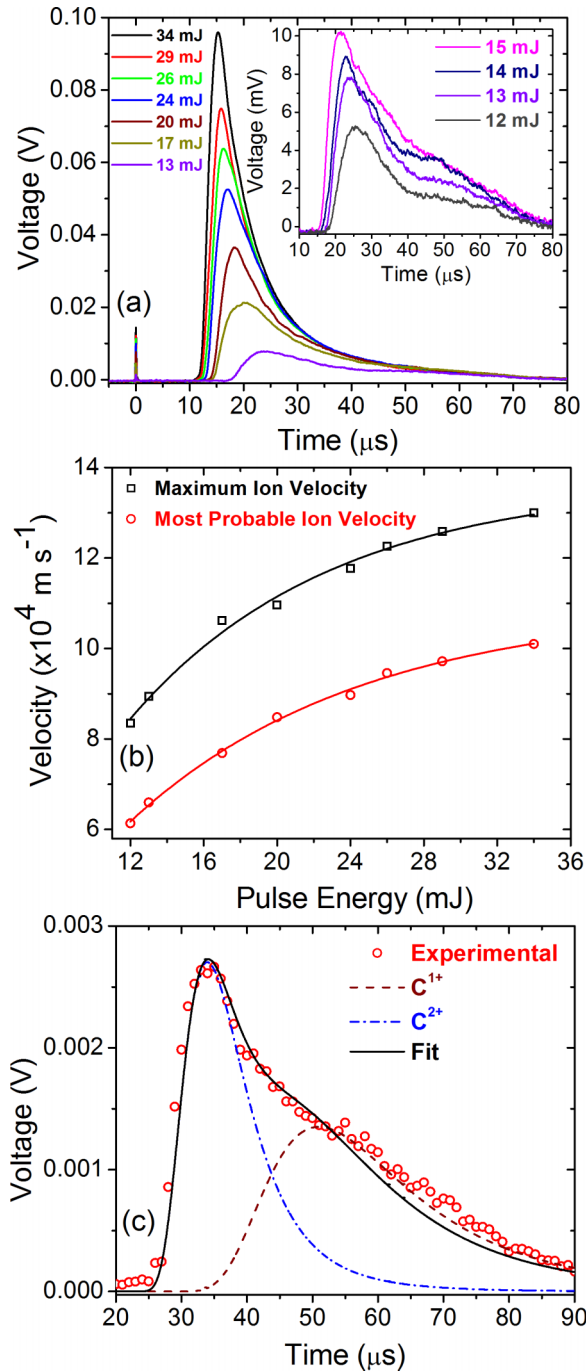
FIG. 3. (a) Time-of-flight ion detection from carbon laser plasma for different laser pulse energies. *Inset*: carbon ion signal components; slow ions start after ~40 μs for the lower laser energies. For laser energies >15 mJ, the shoulder in the TOF signal disappears. (b) Ion velocities for different laser pulse energies. (c) Deconvolution of the carbon ion current recovered by the shifted-Maxwellian fit at pulse energy of ~8 mJ (25 J cm^{-2}).

behavior of TOF signal with increasing laser pulse energy shows that an increase in ion signal with laser pulse energy and a shortened arrival time due to increased ion energy. Below a pulse energy of ~15 mJ, the signal has a double peak form with a shoulder appearing at ~40 μs. This shoulder in the TOF signal disappears within the background at high laser energies. The process of ion acceleration is initiated by electron acceleration by inverse Bremsstrahlung within the laser pulse duration. Due to the slower mobility of ions compared to the electrons, large Coulomb forces are formed between fast electron and ion layers in the early stages of plasma plume formation. The electric field due to the Coulomb forces accelerates ions with higher degree of ionization to higher kinetic energies. The ions with higher kinetic energies are located in the outer position of the plasma plume due to their higher flow velocity.[34] For laser pulse energies higher than 24 mJ (1 × 10^{10} W cm^{-2}), the increase in ion velocity slows down. Fig. 3(b) shows the maximum and most probable ion velocities with the laser energy. For 29 mJ pulse energy, the most probable carbon ion velocity is 9.6 × 10^4 m s^{-1}, corresponding to a kinetic energy of ~570 eV. Ions' kinetic energy increase with increasing laser pulse energy. The carbon ion signal was fitted to a shifted Maxwell–Boltzmann function $I(t) = At^{-5} \exp\left[-m(L/t - u_f)^2/2kT_{eff}\right]$ where A is a normalizing constant, u_f is the flow velocity, and T_{eff} is the effective temperature associated with translational motion along the plume axis.[26] Fig. 3(c) shows the TOF data and corresponding fits. The observed data fit with the shifted Maxwellian-Boltzmann distribution is an indication of the thermalization of the plume particles. The cloud dimension along the target normal can be estimated from $L_0 = u_t\tau$, where τ is the laser pulse duration and u_t is the thermal velocity of the particles given by $u_t = \sqrt{8kT_s/\pi m}$. The surface temperature T_s is given by $T_s = 0.9T_c$, where T_c is the thermodynamic critical temperature.[26] T_c value was given in the literature for graphite to be in the range of 1-1.3 eV.[34] When we take the T_s as 14 000 K, the thermal velocity is calculated as $u_t = 5 \times 10^3$ m/s, and cloud dimension $L_0 = 0.035$ mm, which implies that the plasma is undergoing planar expansion during the laser pulse. Using these parameters, the plume dimension from $L_z = u_f t + L_0$ is ~4 cm at time t = 1 μs. These calculations can be used for estimating angular distribution of accelerated ions from plasma.[30]

3. Focal point dependence

The laser focusing position on the target was found to affect the production of the higher charge state ions. The distance between the focusing lens and the target is 202 mm. The lens was mounted on a linear translational stage to vary the focal point relative to target. Fig. 4 shows the Faraday cup signal at different laser focus positions with a laser pulse energy of ~32 mJ. As the lens is moved so that the focal point position is varied from inside the target (–values) to in front of the target surface (+values), the recorded ion signal is modified. Positioning the lens so that the focal spot is in front of the target by up to ~5.0 mm, the ion signal has earlier arrival times with one significant peak. Beyond ~5 mm, a slow peak appears at ~40 μs which is small compared to the fast
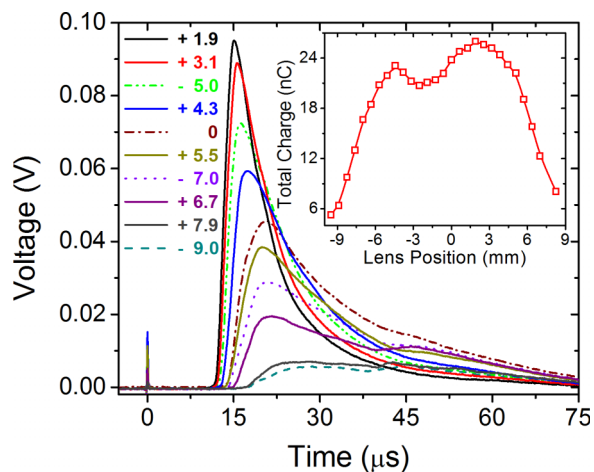
FIG. 4. Carbon plasma ion current signal when the position of lens is varied (mm). *Inset*: total charge change by varying the longitudinal position of the lens.

one. Likewise, with focusing the laser ~7.0 mm inside the target surface, a similar double-peaked signal is observed. The inset in Fig. 4 shows the total charge detected versus the lens position. The ion yield decreases when the laser focal spot is shifted inside the target surface, reaching to its minimum at ~9.5 mm. The maximum ion signal is observed at a lens focal position of ~1.9 mm in front of the target surface which also yields the fastest peak arriving at ~11.9 μs with a maximum velocity of ~1.3 × 10^5 m s^{-1} and total charge of ~26 nC. The ion TOF signal is modified as the lens focusing spot is moved from position that gives the higher yields since, for the low yield positions, the predominant ions are singly and doubly charged. Placing the focus a few mm inside or in front of the target surface results in a larger irradiated area on surface, leading to higher ionization of carbon ions due to slower heat dissipation on a larger surface area during the plasma formation.[13] The dependence of ion yield on the position of the focal spot was discussed for MCI generation from Au, Pb, Ta, and C.[35,36] The larger laser spot area on target results in lower laser power density and, in general, lower ion charge state and energy. However, over a certain focal spot distance away from the target surface, the ion yield is increased due to the larger surface area ablated and the resulting larger volume of the laser plasma.[37] Having the highest power density in the waist of the laser beam does not necessarily result in the highest total number of ions due to the effect of reduced plasma volume.[38] When the focal position is in front of the target surface, the interaction of part of the laser pulse with the generated plasma further heats the expanding plasma and contributes to ion yield. This explains the higher total charge obtained at a lens position of 1.9 mm in front of the target. On the other hand, the plasma propagation angle becomes smaller with increasing spot dimension. Since the Faraday cup is positioned at a fixed angle and location, higher yields of carbon ions are detected. Focusing the laser inside the target has a contribution from the increased spot size only. The lens position was kept at ~1.9 mm in front of the target throughout the study. This focal point location results in the highest ion yield and fastest ion peak arrival time.

B. Ion extraction with external electric field

1. Extraction voltage dependence

For this part of the study, the laser pulse fluence was maintained at 95 J cm^{-2} throughout the measurements. With the target grounded, the carbon ion pulse containing all the charges travels as a bunch with most probable kinetic energy of ~597 eV corresponding to ion velocity of 9.8 × 10^4 m s^{-1}. When an acceleration voltage is applied to the target, ions with different charges spread in time with the higher charge state arriving at the Faraday cup earlier. Neglecting the initial ion velocity from the plasma plume, the TOF for the carbon ions is $t_a + t_d = d\sqrt{2m/zeV} + S\sqrt{m/2zeV}$ where t_a is the acceleration time for an ion from target to the extraction mesh, t_d is the time that ions drift at a constant velocity from extraction mesh to the Faraday cup, d is the distance between target and the extraction mesh, S is the distance from the extraction mesh to the Faraday cup, both in meters, m is the atomic mass of C in kg, z is the charge state, qe is the electron charge, and V is the acceleration voltage applied on the carbon target. The above equation for TOF does not consider the effect of plasma shielding limiting the ion acceleration by the external electric field and the ion acceleration in the expanding plume. The electric field between the grounded mesh and the target does not fully penetrate the plasma plume, thus the ions experience the applied electric field at a location between the target and the grounded mesh, and therefore, are accelerated less than the potential applied to the target. Fig. 5(a) shows the extraction and separation in time of carbon MCIs. Besides the initial velocity from the internal electric field, the carbon ions gain velocity due to the external electric field. Introducing an electric field increases the kinetic energy of ions, thus separation of ions occurs with faster arrival time at the Faraday cup. More electrons are repelled and more ions are exposed to the accelerating field. Space-charge limited flow in the ion sheath governs the ion extraction if the ion density is neglected during ion extraction by the external electric field.[39,40] The inset in Fig. 5(a) shows the accelerated carbon ions at 4 kV voltage applied to target. The ions accelerate according to their z/m ratio. Up to C^{3+} ions are observed. By combining the EIA with TOF energy analyzer, we measured the kinetic energy that the carbon ions gained. Knowing the E/z selection band of the EIA and from the TOF signal detected on the Faraday cup for that selected E/z band, the ion charge state and energies are determined. The Faraday cup signal is shown in Fig. 5(b) for a laser pulse energy of ~30 mJ. The acceleration voltage on target was set to 5, 7, and 9 kV while varying the E/z selection of the EIA to achieve maximum current delivered to the Faraday cup. When 5 kV is applied to target, the ion energy gain per charge z is about 3.2 keV, and up to C^{4+} ions are detected.

In our geometry, the ion acceleration occurs during plasma expansion. The large ion peaks in Fig. 5(a) are the ions separated from the expanding plasma without acceleration. Due to the retrograde forces, the stronger the applied electric field in the target-to-mesh region, the more ions are extracted from the plasma and accelerated.[39] These ions give the signal shown in Fig. 5(b). As the electric field in the target-to-mesh region is increased the extracted ions diverge more and do not
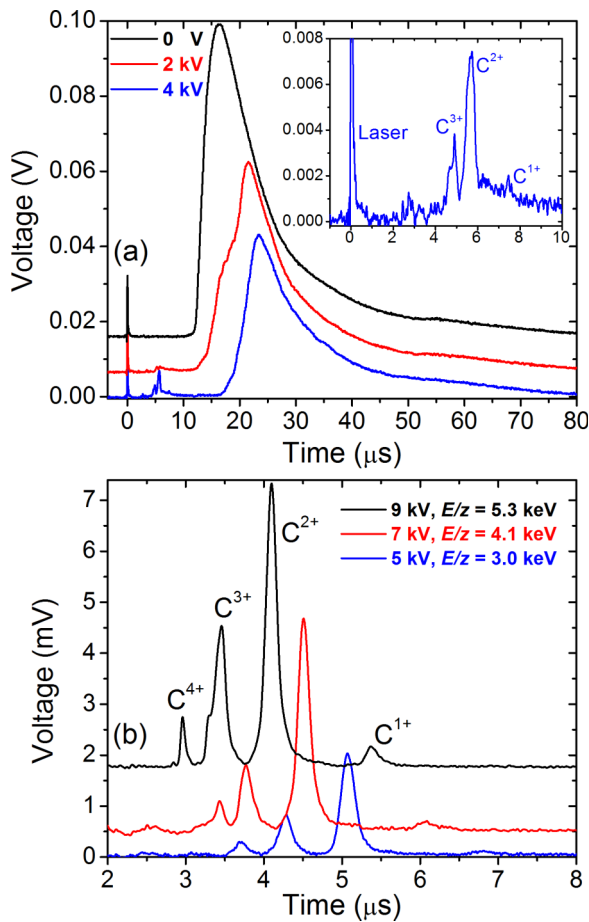
FIG. 5. (a) MCI pulse from the carbon laser plasma. *Inset*: extraction up to C^{3+} at 4 kV acceleration voltage. (b) Total charge and C MCI extraction with acceleration voltage.

FIG. 6. (a) Carbon MCIs detected at different laser pulse energies. Results indicate that up to C^{4+} can be extracted with a laser fluence of 76 J cm^{-2} (24 mJ). (b) Charge detected for each carbon ion.

reach the Faraday cup. The reduction in the plasma ion signal in Fig. 5(a) is due to the ions extracted from which only a portion reaches the Faraday cup. What appears like a shift in the plasma ion peak is due to the extraction of the faster ions in the double-layer region developed in the plasma plume while traversing the target-to-mesh region. Ion energies of about 5.1, 10.6, 13.2, and 18.2 keV were obtained for C^{1+}, C^{2+}, C^{3+}, and C^{4+}, respectively, at 9 kV acceleration voltage. During the early stage of laser plasma expansion, recombination of highly charged ions may occur, which can depress ion yield for higher charge states. The ablated material attenuates the incoming laser radiation as the plasma becomes optically dense at high laser fluences and the plasma absorbs or reflects the later part of the laser pulse.[41] Electron-atom inverse bremsstrahlung and Mie absorption are among the main absorption mechanisms.[42]

2. Laser energy dependence

The MCI detected is strongly dependent on the laser pulse energy which increases the plasma density and temperature allowing for generation of higher state carbon ions. To study the dependence of MCI generation on the laser pulse energy, the acceleration voltage and the EIA selection were kept at 5 kV and $E/z = 3.0$ keV, respectively. The MCI spectrum

obtained at laser pulse energies from 4 mJ (12 J cm^{-2}) to 36 mJ (108 J cm^{-2}) is shown in Fig. 6(a). The threshold energy for the carbon ion generation was found to be $\sim$6 mJ (18 J cm^{-2}). At low laser pulse energies, only C^{1+} and C^{2+} were observed. The average charge state, peak ion energies, and corresponding intensities are increased accordingly with the laser pulse energy. For laser energies of 18 and 24 mJ up to C^{3+} and C^{4+} are observed, respectively. We did not observe C^{5+} or C^{6+} at these laser energies. The reduced TOF time with the laser energy observed in Fig. 6(a) is due to the increase in kinetic energy of the ions drifting out of the expanded plasma. Fig. 6(b) is showing the total charge dependence on laser pulse energy. The total charge detected by the Faraday cup increases with the laser energy with the biggest contribution coming from C^{2+} ions.

3. Focal point dependence

The maximum charge state and the total charge delivered to the Faraday cup increase with the laser pulse energy. The threshold value for the carbon ion generation was found to be dependent on the laser spot size on target. The core temperature decreases more slowly for a larger laser spot size due
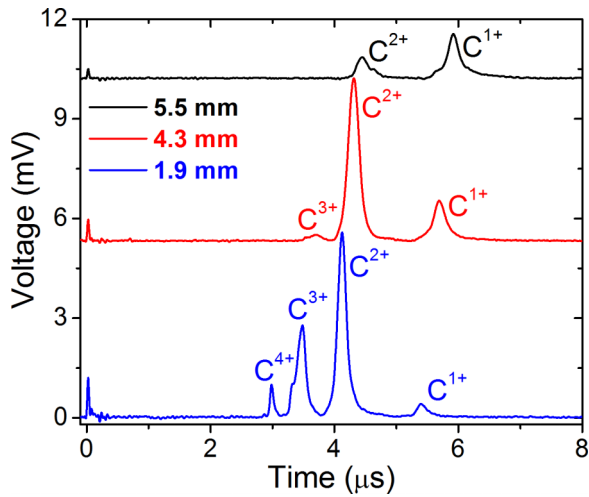
FIG. 7. Carbon ions detected by the Faraday cup when focus is positioned in front of the target's surface.

to the lower thermal diffusivity which decreases the threshold value. The effect of the laser focus position on carbon ion generation is shown in Fig. 7. The voltage applied to the carbon target was 9 kV while the laser pulse energy was ~30 mJ. Higher charge states are detected when the laser is focused in

front of the target surface because larger irradiated area causes slower heat dissipation and changes the angular distribution of ejected carbon ions. At a lens position for a focus ~5.5 mm in front of the target's surface, C^{1+} and C^{2+} ions are detected. Observation of C^{3+} and C^{4+} ions depends more strongly on the laser spot size as both are detected only when the lens is positioned for a focus ~1.9 mm in front of the target's surface. The EIA plates were biased at ±1.25 kV to achieve MCI kinetic energy selection centered at $E/z = 5.3$ keV. The maximum ion charge state of C^{4+} was obtained when the laser radiation was focused at 1.9 mm in front of the target. This optimum position was determined from the measurements shown in Fig. 4. The optimum focus position for ion yield, at 1.9 mm in front of target surface, is consistent with results in the inset of Fig. 4. This is in agreement with previous results.[36] In Fig. 7, the EIA analyzer is set to allow ions with central energy-to-charge ratio of $E/z = 5.3$ keV which corresponds to the maximum of the ion energy distribution for the target biased at 9 kV. For the focus positions of 5.5, 4.3, and 1.9 mm in front of the target, the maximum carbon ions generated are C^{2+}, C^{3+}, and C^{4+}, respectively. We observed a similar trend of ion generation when the laser is focused inside the target. Only C^{1+} and C^{2+} ions are detected when the laser pulse is focused at ~7.0 mm inside the target.
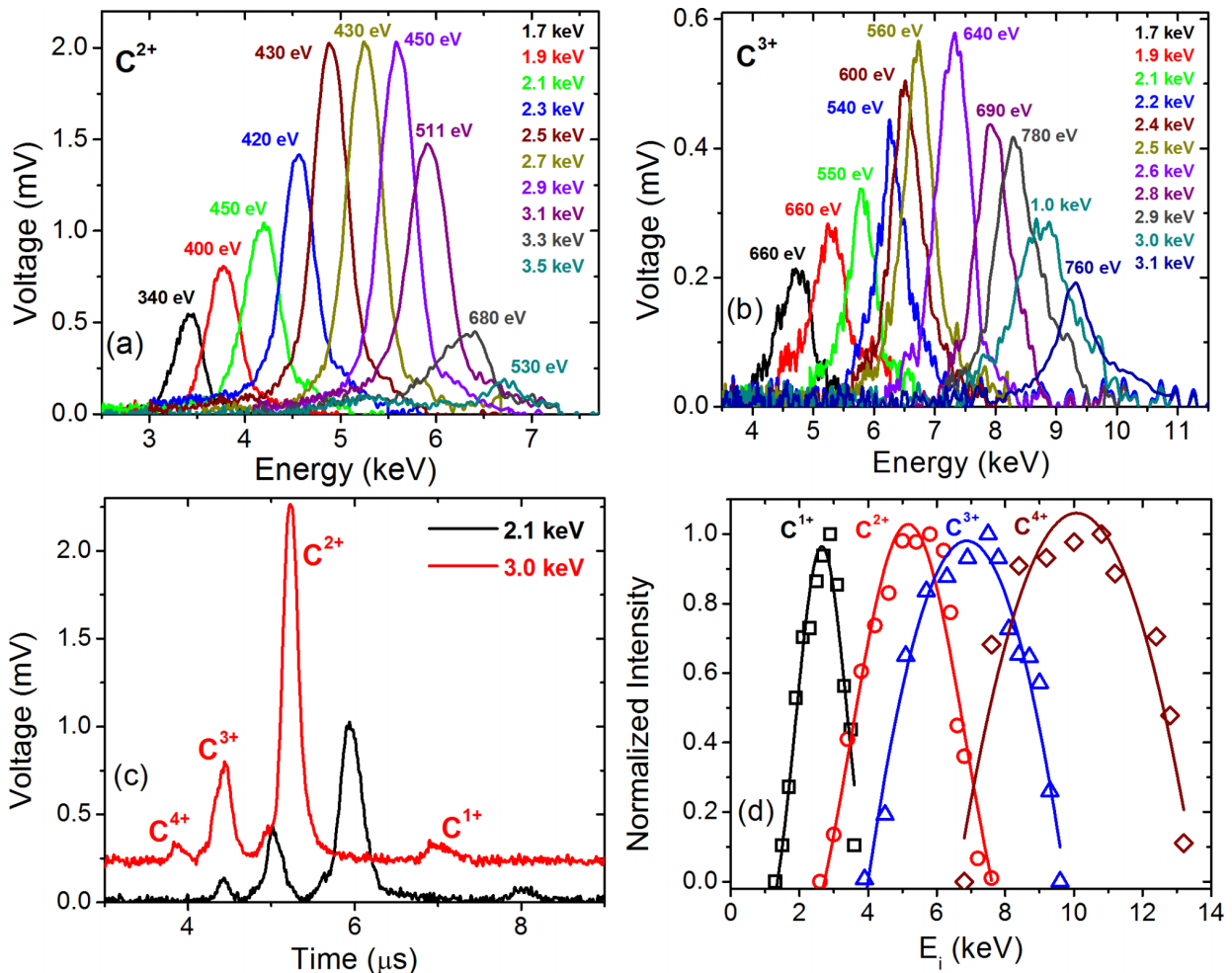
FIG. 8. (a) and (b) Signal for C^{2+} and C^{3+} ions for IEA operated in a range of E/z selection. FWHM values of each curve are presented in eV. FWHM values are stated on top of each curve corresponding to different E/z selection. (c) Carbon ions spectra at two different E/z selections. (d) Ion energy distribution as a function of the charge state.

4. Ion energy distributions

The EIA was used to obtain the energy distribution of the C MCIs. The laser pulse energy was 30 mJ with 5 kV applied to target. The focal position was kept at ~1.9 mm in front of the target. Faraday cup signals were recorded for different E/z ratios in order to construct the MCI energy distribution. The voltage was varied from ±350 to ±900 V on the deflection plates of the EIA to transmit ions with different E/z ratios. Figs. 8(a) and 8(b) show a typical EIA spectrum of the C^{2+} and C^{3+} ions emitted. The signal from C^{2+} and C^{3+} ions was stronger than the signal from C^{1+} and C^{4+}, and therefore, gives more accurate measurement of the resolution of the EIA. Ten distinctive peaks correspond to C^{2+} ions, and eleven distinctive peaks correspond to C^{3+} ions. As the voltage applied to the EIA plates is increased, high energy components of the C^{2+} and C^{3+} ions appear in the energy spectrum. The C^{2+} and C^{3+} intensities are maximum with a kinetic energy of about 2.6 kV/per charge state z. Further increasing the EIA plate voltage shows the more energetic components of the C^{2+} and C^{3+} ions. The peak width of C^{2+} and C^{3+} before the EIA analyzer is ~2.5 μs. The ions seem to be overlapped in time before deflection. The FWHM slightly increases with increasing the E/z as shown on top of each curve in Figs. 8(a) and 8(b). The FWHM for C^{2+} was 340 eV and 530 eV with $E/z = 1.7$ keV and $E/z = 3.5$ keV, respectively. However, the resolution of the EIA ($\Delta E/E$) remains within 7%–10% for the entire range. Using the data collected for a certain E/z, we can reconstruct the carbon ion energy distribution before the EIA. We report this in Fig. 8(c) for all charges detected when the E/z is varied from 2.1 to 3.0 keV. We also report on ion the energy distributions from C^{1+} to C^{4+} in Fig. 8(d) constructed from E/z selection between ~1.7 and ~3.5 keV. The distributions are peaked at about 2.6, 5.1, 7.2, and 10.0 keV in the case of C^{1+}, C^{2+}, C^{3+}, and C^{4+}, respectively. The energy shift is ~2.6 keV per charge z and proportional to z. The ions are accelerated with respect to their charge, their state and shifted towards the higher energy according to the Coulomb-Boltzmann shifted model.[43]

IV. CONCLUSIONS

We have analyzed MCI generated from carbon laser plasma in terms of the ion charge state and energy distribution. The ion charge states and corresponding kinetic energies are increased with the laser energy. The focusing lens position was found to have a strong influence on the generation of higher charge states. A shifted Maxwell–Boltzmann fitting to the ion signal was found to best fit the TOF signal and the retarding field analysis. This approach gives a more accurate deconvolution of the signal from each charge than can be obtained solely from the TOF signal. This fitting indicates ions with multiple charge states exist in the ablation plume where ablation velocity is found to be $u_f = 4 \times 10^4$ m/s, or 99 eV as ablation energy. Considering that the ions with different charges have energies corresponding to the sum of that due to the adiabatic expansion $E_{ablation}$ plus energy gain due to acceleration in the double layer by the Coulomb potential $E_{Coulomb}$, the ion energy E was calculated by $E = E_{ablation} + zE_{Coulomb}$, where z is the ion charge. By fitting this equation to the experimental results with retardation voltage analysis, we estimated the ablation and coulomb energies as 80 and 195 eV, respectively. The plasma cloud dimension was estimated as $L_0 = 0.035$ mm with a plume dimension as 4 cm at time t = 1 μs. When a voltage is applied to the target to establish an external accelerating electric field, ion extraction is observed to be enhanced with the increased electric field. Carbon MCI up to C^{4+} is observed with a relatively low laser fluence of 76 J cm^{-2} and the accelerating voltage of 5 kV. The mean energy of the ions increases with the increase of the ionization state and acceleration voltage. Using the EIA, we have measured the ions energy distributions through E/z selection.

[1]J. D. Gillaspy, J. Phys. B: At., Mol. Opt. Phys. **34**, R93 (2001).

[2]F. Aumayr and H. Winter, Philos. Trans. R. Soc. A **362**, 77 (2004).

[3]M. Muramatsu and A. Kitagawa, Rev. Sci. Instrum. **83**, 02B909 (2012).

[4]T. Meguro, K. Kobashi, T. Ishii, N. Tsuji, Y. Yamamoto, H. Takai, and M. Iwaki, Surf. Coat. Technol. **201**, 8452 (2007).

[5]T. Lu, Y. Qiao, and X. Liu, Interface Focus **2**, 325 (2012).

[6]P. D. Townsend, J. C. Kelly, and N. E. W. Hartley, *Ion Implantation, Sputtering and Their Applications* (Academic Press, London, 1976).

[7]V. Le Roux, G. Machicoane, S. Kerdiles, R. Laffitte, N. Bèchu, L. Vallier, G. Borsoni, M. L. Korwin-Pawlowski, P. Roman, C.-T. Wu, and J. Ruzyllo, J. Electrochem. Soc. **151**, G76 (2004).

[8]S. Gammino, "Production of high-intensity, highly charged ions," in *26th CAS-CERN Accelerator School: Ion Sources, Senec, Slovakia, 29 May-8 June 2012*, edited by R. Bailey (CAS-CERN, 2012), pp. 123–164.

[9]H. Daido, M. Nishiuchi, and A. S. Pirozhkov, Rep. Prog. Phys. **75**, 056401 (2012).

[10]W. Mróz, J. Wolowski, E. Woryna, B. Králiková, J. Krása, L. Láska, K. Mašek, J. Skála, K. Rohlena, O. B. Shamaev, B. Y. Sharkov, H. Haseroth, K. L. Langbein, and T. R. Sherwood, Rev. Sci. Instrum. **65**, 1272 (1994).

[11]M. H. A. Shaim and A. H. E. Elsayed, Nucl. Instrum. Methods Phys. Res., Sect. B **356**, 75 (2015).

[12]T. Henkelmann, G. Korschinek, G. Belayev, V. Dubenkov, A. Golubev, S. Latyshev, B. Sharkov, A. Shumshurov, and B. Wolf, Rev. Sci. Instrum. **63**, 2828 (1992).

[13]V. Nassisi, A. Pedone, and A. Rainò, Nucl. Instrum. Methods Phys. Res., Sect. B **188**, 267 (2002).

[14]A. Lorusso, J. Krása, K. Rohlena, V. Nassisi, F. Belloni, and D. Doria, Appl. Phys. Lett. **86**, 081501 (2005).

[15]H. Kashiwagi, M. Fukuda, M. Okamura, R. A. Jameson, T. Hattori, N. Hayashizaki, K. Sakakibara, J. Takano, K. Yamamoto, Y. Iwata, and T. Fujimoto, Rev. Sci. Instrum. **77**, 03B305 (2006).

[16]M. Okamura, R. A. Jameson, H. Kashiwagi, T. Hattori, N. Hayashizaki, K. Sakakibara, K. Yamamoto, and T. Kanesue, Radiat. Eff. Defects Solids **160**, 445 (2005).

[17]R. C. Constantinescu, S. Hunsche, H. B. van Linden van den Heuvell, H. G. Muller, C. LeBlanc, and F. Salin, Phys. Rev. A **58**, 4637 (1998).

[18]S. Witanachchi, A. M. Miyawa, and P. Mukherjee, Mater. Res. Soc. Symp. Proc. **617**, 1–6 (2000).

[19]L. Torrisi, F. Caridi, D. Margarone, A. Picciotto, A. Mangione, and J. J. Beltrano, Appl. Surf. Sci. **252**, 6383 (2006).

[20]S. I. Okihara, M. Fujimoto, H. Takahashi, K. Matsukado, S. Ohsuka, S. I. Aoshima, S. Okazaki, T. Ito, and Y. Tsuchiya, Appl. Phys. Lett. **89**, 121502 (2006).

[21]C. Cher-Liang, C. Eng-Fong, G. Hao, A. J. Bourdillon, J. Yu-Min, P. Jin-Sheng, Z. An-Qing, and C. Lap, Appl. Phys. Lett. **75**, 355 (1999).

[22]C. Pierret, L. Maunoury, I. Monnet, S. Bouffard, A. Benyagoub, C. Grygiel, D. Busardo, D. Muller, and D. Höche, Wear **319**, 19 (2014).

[23]H. A. Ching, D. Choudhury, M. J. Nine, and N. A. A. Osman, Sci. Technol. Adv. Mater. **15**, 014402 (2014).

[24]V. Marx, Nature **508**, 133 (2014).

[25]M. Durante and J. S. Loeffler, Nat. Rev. Clin. Oncol. **7**, 37 (2010).

[26]N. M. Bulgakova, A. V. Bulgakov, and O. F. Bobrenok, Phys. Rev. E **62**, 5624 (2000).

[27]M. M. Abdelrahman, Sci. Technol. **2**, 98 (2012).

[28]C. Farnell, C. Farnell, S. Farnell, and J. Williams, "Electrostatic analyzers with application to electric propulsion testing," in *Proceedings of the 33rd International Electric Propulsion Conference*, *Washington, DC*, *6–10 October 2013* (Electric Rocket Propulsion Society, 2013), pp. 1–48, http://apapes. physics.uoc.gr/references/Farnell_IEPC-2013-300_ESA.pdf.

[29]D. Mascali, S. Tudisco, N. Gambino, A. Pluchino, A. Anzalone, F. Musumeci, A. Rapisarda, and A. Spitaleri, Europhys. Lett. **100**, 45003 (2012).

[30]L. Torrisi, S. Cavallaro, M. Rosinski, V. Nassisi, V. Paperny, and I. Romanov, Nukleonika **57**, 323 (2012), http://yadda.icm.edu.pl/baztech/ element/bwmeta1.element.baztech-article-BUJ8-0023-0013.

[31]R. Kelly and R. W. Dreyfus, Surf. Sci. **198**, 263 (1988).

[32]A. Miotello and R. Kelly, Appl. Surf. Sci. **138-139**, 44 (1999).

[33]S. S. Harilal, C. V. Bindhu, R. C. Issac, V. P. N. Nampoori, and C. P. G. Vallabhan, J. Appl. Phys. **82**, 2140 (1997).

[34]H. Horisawa and I. Kimura, Vacuum **65**, 389 (2002).

[35]E. Woryna, P. Parys, J. Wolowski, L. Laska, J. Krasa, K. Masek, M. Pfeifer, B. Kralikova, J. Skala, P. Straka, and K. Rohlena, Appl. Phys. Lett. **69**, 1547 (1996).

[36]J. Krása, A. Velyhan, D. Margarone, E. Krouský, J. Ullschmied, J. Skála, L. Láska, K. Jungwirth, and K. Rohlena, Rev. Sci. Instrum. **81**, 02A504 (2010).

[37]L. Láska, J. Krása, M. Pfeifer, K. Rohlena, S. Gammino, L. Torrisi, L. Andò, and G. Ciavola, Rev. Sci. Instrum. **73**, 654 (2002).

[38]L. Láska, K. Jungwirth, B. Králiková, J. Krása, M. Pfeifer, K. Rohlena, J. Skála, J. Ullschmied, J. Badziak, P. Parys, J. Wolowski, E. Woryna, S. Gammino, L. Torrisi, F. P. Boody, and H. Hora, Plasma Phys. Controlled Fusion **45**, 585 (2003).

[39]F. F. Chen, Phys. Fluids **25**, 2385 (1982).

[40]K. Yamada and T. Tetsuka, J. Nucl. Sci. Technol. **31**, 301 (1994).

[41]R. Rozman, I. Grabec, and E. Govekar, Appl. Surf. Sci. **254**, 3295 (2008).

[42]T. Moscicki, J. Hoffman, and Z. Szymanski, Arch. Mech. **63**(2), 99 (2011), http://www.ippt.pan.pl/Repository/o361.pdf.

[43]L. Torrisi, S. Gammino, A. Picciotto, D. Margarone, L. Laska, J. Krasa, K. Rohlena, and J. Wolowski, Rev. Sci. Instrum. **77**, 03B708 (2006).